UNIVERSITY
OF WOLLONGONG
AUSTRALIA

University of Wollongong
Research Online

Australian Institute for Innovative Materials - Papers | Australian Institute for Innovative Materials

2017

Improved Reversibility of Fe^{3+}/Fe^{4+} Redox Couple in Sodium Super Ion Conductor Type Na3Fe2(PO4)3 for Sodium-Ion Batteries

Ranjusha Rajagopalan
University of Wollongong, rr876@uowmail.edu.au

Bo Chen
Nanyang Technological University

Zhicheng Zhang
Nanyang Technological University

Xing Long Wu
Nanyang Technological University

Yonghua Du
Institute of Chemical and Engineering Sciences, Singapor

See next page for additional authors

Publication Details

Rajagopalan, R., Chen, B., Zhang, Z., Wu, X., Du, Y., Huang, Y., Li, B., Zong, Y., Wang, J., Nam, G., Sindoro, M., Dou, S. Xue., Liu, H. Kun. & Zhang, H. (2017). Improved Reversibility of Fe^{3+}/Fe^{4+} Redox Couple in Sodium Super Ion Conductor Type Na3Fe2(PO4)3 for Sodium-Ion Batteries. Advanced Materials, 29 (12), 1605694-1.

Research Online is the open access institutional repository for the University of Wollongong. For further information contact the UOW Library: research-pubs@uow.edu.au

Improved Reversibility of Fe^{3+}/Fe^{4+} Redox Couple in Sodium Super Ion Conductor Type Na3Fe2(PO4)3 for Sodium-Ion Batteries

Abstract

The methodology employed here utilizes the sodium super ion conductor type sodium iron phosphate wrapped with conducting carbon network to generate a stable Fe3+/Fe4+ redox couple, thereby exhibiting higher operating voltage and energy density of sodium-ion batteries. This new class of sodium iron phosphate wrapped by carbon also displays a cycling stability with >96% capacity retention after 200 cycles.

Disciplines

Engineering | Physical Sciences and Mathematics

Publication Details

Rajagopalan, R., Chen, B., Zhang, Z., Wu, X., Du, Y., Huang, Y., Li, B., Zong, Y., Wang, J., Nam, G., Sindoro, M., Dou, S. Xue., Liu, H. Kun. & Zhang, H. (2017). Improved Reversibility of Fe^{3+}/Fe^{4+} Redox Couple in Sodium Super Ion Conductor Type Na3Fe2(PO4)3 for Sodium-Ion Batteries. Advanced Materials, 29 (12), 1605694-1.

Authors

Ranjusha Rajagopalan, Bo Chen, Zhicheng Zhang, Xing Long Wu, Yonghua Du, Ying Huang, Bing Li, Yun Zong, Jie Wang, Gwang-Hyeon Nam, Melinda Sindoro, Shi Xue Dou, Hua-Kun Liu, and Hua Zhang

This journal article is available at Research Online: http://ro.uow.edu.au/aiimpapers/2425

Improved Reversibility of Fe^{3+}/Fe^{4+} Redox Couple in Sodium Super Ion Conductor-Type $Na_3Fe_2(PO_4)_3$ for Sodium-Ion Batteries

Ranjusha Rajagopalan, Bo Chen, Zhicheng Zhang, Xing-Long Wu, Yonghua Du, Ying Huang, Bing Li, Yun Zong, Jie Wang, Gwang-Hyeon Nam, Melinda Sindoro, Shi Xue Dou, Hua Kun Liu,* Hua Zhang**

[*] Dr. R. Rajagopalan, B. Chen, Dr. Z. Zhang, X.-L. Wu, Y. Huang, J. Wang, G.-H. Nam, Dr. M. Sindoro, Prof. H. Zhang

Center for Programmable Materials, School of Materials Science and Engineering, Nanyang Technological University, 50 Nanyang Avenue, Singapore 639798, Singapore

E-mail: HZhang@ntu.edu.sg; hzhang166@gmail.com

Website: http://www.ntu.edu.sg/home/hzhang/

Dr. R. Rajagopalan, Prof. S. X. Dou, Prof. H. K. Liu

Institute for Superconducting and Electronic Materials, University of Wollongong, Wollongong, NSW 2522, Australia

E-mail: hua@uow.edu.au, shi@uow.edu.au

X.-L. Wu,

National and Local United Engineering Lab for Power Battery, Department of Chemistry, Northeast Normal University, Changchun, Jilin 130024, P.R. China

Dr. Y. Du

Institute of Chemical & Engineering Sciences, A*STAR, 1 Pesek Road, Jurong Island, 627833, Singapore

Dr. B. Li, Dr. Y. Zong

Institute of Materials Research and Engineering (IMRE), A*STAR (Agency for Science, Technology and Research), 2 Fusionopolis Way, Innovis #08-03, Singapore 138634, Singapore

Keywords: Sodium iron phosphate, specific capacity, Fe^{3+}/Fe^{4+} redox couple, sodium-ion batteries, cycling

Searching the portable, high energy and safe storage technologies for lithium-ion batteries (LIBs) remains one of the paramount motivations for material researchers.[1] Until now, new cost-effective electrode materials have been used in the large-scale rechargeable LIBs.[2] As one classic example, the olivine-structured $LiFePO_4$ cathode has risen to prominence as a key material for batteries in many commercial applications.[2] The $LiFePO_4$ exhibits specific capacity as high as 140−160 mAh g^{-1} with excellent cycling performance.[2,3] However, compared to layered oxides, the energy density of $LiFePO_4$ is limited by the low operating voltage due to the low potential of Fe^{2+}/Fe^{3+} redox couple. The reversible redox couple of Fe^{3+}/Fe^{4+}, which can provide a higher operating voltage and subsequently a higher specific energy density, has not been successfully demonstrated in LIBs. This is mainly because the +4 oxidation state is not common for iron and a stable Fe^{4+} state was only found in a few examples such as perovskites and related oxides. [4,5] Furthermore, from a battery manufacturer standpoint, a prime importance is always given to the material abundance, while designing an electrode, i.e. iron, which is an abundant element in nature whilst lithium is not. As a natural course, researchers have started to focus on the iron-based cathode materials for rechargeable sodium-ion batteries (SIBs) because both sodium and iron are some of the most abundant and nontoxic materials found in nature. [6,7] Unlike in LIBs, the reversibility of Fe^{3+}/Fe^{4+} redox couple in layered oxides during the sodium intercalation/de-intercalation has been shown in iron-based SIBs. For instance, Kikkawa et al. [8] have demonstrated the sodium de-intercalation from the layered α-$NaFeO_2$, resulting in the formation of Fe^{4+}. Moreover, Takeda et al. [9] used the Mössbauer spectroscopy to confirm the generation of Fe^{4+} species in an electrochemically charged α-$NaFeO_2$ half-cell using lithium metal as a counter electrode. As known, the formation of a reversible Fe^{3+}/Fe^{4+} redox couple from α-$NaFeO_2$ versus Na/Na^+ was first reported by Okada and co-workers. [10] This half-cell was cycled from 3.6 to 1.5 V to obtain the initial specific capacity of 80 mAh g^{-1}. Recently, Komaba and co-workers [6] synthesized the P_2-$Na_x[Fe_{1/2}Mn_{1/2}]O_2$, that utilizes Mn^{3+}/Mn^{4+} and Fe^{3+}/Fe^{4+} redox couples

to reach capacity of ~190 mAh g^{-1}. Though promising, both α-$NaFeO_2$ and P_2-type $Na_x[Fe_{1/2}Mn_{1/2}]O_2$ suffered from the poor capacity retention which was mainly due to the chemical instability of these electrodes at higher operating voltages.[11] Therefore, in order to achieve higher electrode potential coupled with good reversibility, new iron-based structures should be prepared by taking advantage of their higher oxidation states. Unfortunately, there is no report on the Fe^{3+}/Fe^{4+} redox couple in the sodium super ion conductor (NASICON) sodium iron phosphate-based materials for SIBs.

NASICON-type materials have been considered as promising electrode materials for stable SIBs owing to their open three-dimensional (3D) framework feature, high ionic conductivity, and a small volume change (phase related) during the sodium intercalation/de-intercalation processes. However, these materials show inherently low electronic conductivity. [12] Some of methods used for enhancing the ion- and electron-transport kinetics in battery electrodes include designing new materials, nanostructure engineering, functionalized conductive coatings, *etc.* Among them, NASICON materials coated with carbon layers are attractive in improving both the rate capability and the cycling stability. [12] Nevertheless, the thick carbon coating could inhibit the migration of Na^+ ions through the interface between electrode and electrolyte. Due to this delicate balance, one of the most promising strategies is to confine the electrode material within a uniformly thin carbon sheath, forming a percolating 3D conducting network.

In order to combine all of the aforementioned advantages, herein, we discuss a new class of cathode based on $Na_3Fe_2(PO_4)_3$, referred to as SIP. The present work also tries to understand the mechanisms involved for the better reversibility of Fe^{3+}/Fe^{4+} redox potential system at ~3.4 V (*vs.* Na/Na^+) when compared to other reported iron-based poly-anion frameworks, such as Na_2FePO_4F (~3.2V), [13] $Na_2FeP_2O_7$ (3 V), [14] $NaFePO_4$ (~2.7 V), [15] and $Na_4Fe_3(PO_4)_2(P_2O_7)$ (3.2 V) [1] used for SIBs (Supporting **Table 1**). [1, 13–20]

The unsuccessful exploitation of cathodes based on the Fe^{3+}/Fe^{4+} redox couple in LIBs can be mainly attributed to the unmatched electrochemical potential (μ, >4.3 V), which is greater than the potential window of commonly used electrolytes. [21] On the other hand, this redox potential position can be exploited for SIBs because of the 0.3 V lower reduction potential position of Na/Na^+ as compared to the Li/Li^+ counterpart. This has motivated researchers to explore sodium iron-based layered oxides, in which the Fe^{3+}/Fe^{4+} redox couple has been successfully exploited at higher voltage of ~3.3 V. [11] However, these layered oxides still show unsatisfactory cycle performance, which can be attributed to the low stability of octahedrally coordinated Fe^{4+} species that undergoes spontaneous reduction to Fe^{3+} in the charged state. These Fe^{3+} ions, which have zero octahedral field stabilization energy, migrate to the face-shared tetrahedral sites because of the sufficiently high concentration of sodium vacancies created during the de-intercalation process. The tetrahedral Fe^{3+} ions not only hinder the diffusion of sodium by blocking the in-plane octahedral−tetrahedral−octahedral pathway, but also cause the O_3 structure pinning effect. This pinning effect can prevent the overall layer rearrangement to the P_3 phase (required for stable reversibility) and result in the non-equilibrium phase transition. This unique phase transition and the cycle-to-cycle accumulation of migrated Fe species out of their original sites result in a gradual phase degradation, from the ideal layered structure to a more disordered structure. This Phase degradation causes the lowering of equilibrium potential for the Na intercalation.[11] Unlike the traditional layered structure, NASICON with a formula of $Na_3M_2(XO_4)_3$ (M=Fe and X=P in this work) offers a flexible 3D open framework with corner sharing MO_6 and XO_4 polyhedral arranged in the so-called "lantern units" of $[M_2(XO_4)_3]$, hence, providing a better phase stability during the intercalation/de-intercalation process.[22] In this study, the phase purity of synthesized NASICON-type $Na_3Fe_2(PO_4)_3$ (SIP, the detailed synthesis method in the supporting information (SI)) was confirmed by the powder X-ray diffraction (XRD) pattern (PDF card No.: 00-045-0319) (**Figure 1**a). The pattern exhibited the Cc space group,

confirming that [$Fe_2(PO_4)_3$] is formed via interlinking of FeO_6 octahedral and PO_4 tetrahedral units. These lantern units arrange themselves into a highly covalent open structure, exhibiting large interstitial channels through which Na^+ ions can easily diffuse. However, some other small peaks also appeared, which came from the very small amount impurity, i.e. the monoclinic SIP crystal (PDF card No.: 00-033-1251) with Cc space group, obtained in the synthesis of NASICON-type SIP. The diffusion of Na^+ ions within the NASICON structure is anticipated to happen in 3 different ways: 1) through the channel between two PO_4 tetrahedral units, 2) through the voids between a PO_4 tetrahedron and a FeO_6 octahedron, and 3) following a curved pathway to bypass the octahedron into the voids/channels between the adjacent PO_4 tetrahedron and FeO_6 octahedron.[23] Although two different oxygen-environment interstitial sites of Na^+ ions, *i.e.* Na(I) (six-fold coordination situated between two adjacent lantern units) and Na(II) (eight-fold coordination between two PO_4 tetrahedral), can cause the phase change, it only induces minor rearrangement in the NASICON framework. That is, the size of Na(I) anti-prismatic cavity increases as it is being vacated, but the size of FeO_6 octahedron and the Fe-Fe distance within the lantern unit essentially remain the same. Reasonably, we can anticipate that this unaltered open 3D framework can contribute an un-interrupted fast chemical diffusion, better rate capability, and cycling performance, [22] when coupled with a percolating network of conducting carbons as current collectors. For this purpose, the oleic acid was used as a carbon-rich source. After it was annealed with SIP, the obtained sample was designated as SIP-C, in which the carbon amount was optimized to be 1.7 wt%, which will be explained below. In this study, this optimized SIP-C sample was used for all the structural and phase characterizations along with the pure SIP sample. After treated at 750 °C, the oleic acid did not reveal any additional peaks associated with secondary carbon phases (Figure 1a). Since the presence of carbon was not detectable using XRD, the Fourier transform infrared spectroscopy (FT-IR), Raman, and X-ray photoelectron spectroscopy (XPS) were performed to understand the effect and function of carbon in SIP-C samples.

As shown in Figure 1b, the FT-IR spectrum of SIP showed predominant overlapping of ν_1 and ν_3 stretching modes of $(PO_4)^{3-}$ in the range from 1300 to 700 cm^{-1}. Multiple peaks between 650 and 400 cm^{-1} are ascribed to the deformation of O-P-O angle due to the ν_2 and ν_4 bending modes. The peak around 630 cm^{-1} presents the vibrational bonds between Fe^{3+} and O^{2-} in the isolated FeO_6 octahedral structures. The band at 936 cm^{-1} is attributed to the external modes comprised of Na^+, Fe^{3+}, and PO_4^{3-} translations as well as the pseudo rotation motions. The presence of O–C–O asymmetric stretching at 2350 cm^{-1} and C=O vibrations at 1684 cm^{-1} in the SIP-C sample indicates that the carbon is bonded to the SIP structure after the treatment of SIP with oleic acid.

As shown in **Figure 2**a, the XPS peaks at binding energy of 710 and 723 eV indicate the presence of Fe $2p_{3/2}$ and Fe $2p_{1/2}$ orbitals, demonstrating the Fe^{3+} oxidation state. The sharp peak at 531 eV presents O 1s in the $(PO_4)^{3-}$ group. The P 2p peak at 134 eV and the P 2s peak at 195 eV reveal the presence of tetrahedral $(PO_4)^{3-}$ phosphate groups in the sample. The peaks at 1071, 497, 61 and 39 eV indicate Na in the SIP sample. The C 1s peak at 284 eV was de-convoluted to clarify the nature of carbon in the SIP-C sample (Figure 2b). The 3 distinct de-convoluted peaks at binding energies of 284.5, 285.6, and 288.4 eV indicate the presence of C–C, C–O, and O–C=O bonds, respectively. The lower intensities of the C–O and O–C=O bonds as compared to that of C–C bond indicate that the electrical conductivity of these carbons came from the delocalized π-electrons. The Raman analysis (Figure 2c) of the SIP-C showed two high intensity peaks at 1353 and 1592 cm^{-1}, corresponding to the D and G bands of carbon, respectively. In addition, the band at 488 cm^{-1} corresponds to the deformation vibrations of the PO_4 tetrahedral unit in the SIP-C, [24] while the 953 and the 1021 cm^{-1} bands present the vibration of the valence bonds of PO_4. [3– 24, 25] The predominance of the vibrational bands of PO_4^{3-} anions can be attributed to the correlation effect induced by the coupling of PO_4^{3-} with Fe-O units. [24]

Figure 3a shows the scanning electron microscopy (SEM) image of the pristine SIP powder, exhibiting irregularly agglomerated particles. Upon annealing the SIP power with the oleic acid, the resultant SIP-C powder showed porous interconnected flaky morphology (Figure 3b). The transmission electron microscopy (TEM) image showed that the SIP is wrapped by carbon (Figure 3c). The selected area electron diffraction (SAED) patterns (inset of Figure 3c) showed bright diffraction spots in the Debye ring with inter-planar spacing of ~0.37 nm, corresponding to the (021) plane of SIP and the Debye ring with inter-planar spacing of ~0.34 representing the (002) plane of graphitic carbon. [26, 27] The TEM image and the corresponding SAED pattern of the pristine SIP powder are shown in **Figure S1**a and inset of Figure S1a, respectively. The high-resolution (HRTEM) image (Figure 3d) and the corresponding fast Fourier transform (FFT) pattern (inset of Figure 3d) of the SIP-C clearly showed lattice fringes in SIP with lateral *d*-spacings of ~0.31 and 0.37 nm, corresponding to the monoclinic ($\bar{2}22$) and (021) planes, respectively. Furthermore, Figure S1b shows the clear lattice fringes of this graphitic carbon in SIP-C.

To verify the elemental distribution of SIP-C powder, spatial elemental mapping for Na, Fe, P, O, and C was carried out (Figure 3e), which confirmed that the darker structure in the TEM image (Figure 3c) is SIP with overlaying C signals due to the carbon wrapping. The carbon wrapping on SIP might arise from the decarbonylation of oleic acid during the annealing process, which in turn led to the formation of CO and H_2O. The resultant CO can reduce the exposed Fe_2O_3 surface to metallic Fe. At temperature of ~750 °C, Fe exhibits the face centered cubic (FCC) structure. [28] It is anticipated that carbon atoms can be easily held within this loosely packed structure, forming solid solution. A slow cooling rate used in the present study allows the sufficient time for Fe atoms to rearrange into the body centered cubic (BCC) structure.[29] Due to the lower solubility of carbon in BCC structure as compared to the FCC structure, the BBC structure cannot hold as many carbon atoms as FCC structure and let the carbon precipitate as thin layers.[29] By the virtue of mismatch of the coefficient of thermal

expansion between carbon and Fe, these thin carbon layers experience tension leading to wrapping of the formed SIP. Although we can modulate the amount of oleic acid to get different weight percentages of carbon (**Figure S2**a) in SIP, the best specific discharge capacity (at 0.1 C rate in the potential range of 1.5–4.2 V (*vs.* Na^+/Na)) was obtained when the carbon content was maintained at weight percent of ~1.7 (Figure S2b). Therefore, the following electrochemical characterization was performed on this optimized SIP-C electrode with carbon of 1.7 wt%.

The rate capability of the SIP-C sample was compared with the pristine SIP in the potential range of 1.5–4.2 V (*vs.* Na^+/Na) at different C-rates (**Figure 4**a). The theoretical specific capacity and specific energy density in the given potential range were found to be ~115 mAh g^{-1} and ~326 Wh kg^{-1}, respectively. The discharge specific capacity of SIP-C and SIP decreased from 109 to 75 mAh g^{-1} and from 84 to 23 mAh g^{-1}, respectively, when the C rate increased from 0.1 to 5 C. The average coulombic efficiencies of both cells were observed to be > 90% at different C rates (Figure 4b). This better columbic efficiency indicates the less secondary parasitic reactions arising from the decomposition of electrolyte or other phase changing redox reactions in the battery.[30,31] Decreasing in the specific capacity with increasing C rate, as observed in rate capability study, could be attributed to the reduced participation of the active SIP sites during the fast charge/discharge process and the poor current collection properties of the electrode, where the electrons recombine from the excited state to the ground state before they reach the external circuit. However, in the SIP-C electrode, this electron transportation is facilitated by the presence of carbon which provides percolating conducting pathways from the electrode/electrolyte interface to the external circuit, resulting in an improved rate capability compared to their pristine SIP. The principal electron transport mechanism in this carbon network depends on the sp^2-hybridized carbon atoms (see the high intensity (C─C) peak in Figure 2b) with the delocalized π-electrons to form an interacting percolating pathway, which provides the smooth electron transportation

and results in better electronic conductivity. This can be corroborated from the Nyquist plot of the SIP and the SIP-C cells (Figure 4c). The charge transfer resistance (R_{ct}: diameter of the semicircle on the x-axis) reduced from 410 Ω (SIP) to 193 Ω (SIP-C), indicating an easier transport of electrons/ions through the electrode/electrolyte interface in SIP-C. Moreover, the four-probe measurement also confirmed the resistance reduction in SIP-C. The pristine SIP sample showed a sheet resistance of ~14.5 × 10^3 Ω sq^{-1} which is ~7 times that of SIP-C (~2.1 × 10^3 Ω sq^{-1}). Figure 4d shows the specific discharge capacity of the SIP and SIP-C at 1 C rate in the first 200 cycles. The initial specific discharge capacities of the SIP and SIP-C were estimated to be ~61 and 96 mAh g^{-1}, respectively. The capacity retentions in the SIP and SIP-C samples were found to be ~80 % and 96 %, respectively, after 200 cycles. Compared to the previous reports, the capacity retention of our SIP-C sample is better (Supporting Table 1). In addition, the cycling performance of pristine SIP is better than the previously reported Fe^{3+}/Fe^{4+} based cathodes which could be attributed to the flexible 3D open framework of SIP compared to the layered or the olivine systems. [10,11] Importantly, the coulombic efficiency was consistently maintained at > 90% for both SIP and SIP-C samples during this prolonged cycling (**Figure S3**). The capacity fading could be attributed to three major factors: [30] 1) degradation of electrolyte at high operating potential, 2) dissolution of the electrode into electrolyte, and 3) dimensional or structural variations within the electrode during the cycling. During the cycling, the volumetric expansion/contraction, causing the SIP matrix to be stretched and relaxed, is anticipated in the electrode. This leads to the formation of microscopic tensile and compressive stress in the entire electrode. However, in the SIP-C sample, the presence of percolating carbon can distribute these microscopic stresses along the electrode matrix. The bridging of these carbon layers over each other could also increase the shear strength of the electrode, which in turn may help to prevent the crack formation and avoid any peeling or delamination under cycling. In this study, the carbon phase can also prevent the agglomeration and degradation of active particles by forming a protective layer

during the prolonged charging and discharging, leading to the improved cycling stability. However, in the pristine SIP electrode, during cycling, the particles tend to oscillate relative to their original positions. The microscopic stress generated during cycling in such dense and agglomerated SIP electrode matrix will have the tendency to undergo mechanical fatigue and fracture of the SIP electrode particles. [31] As a consequence, these SIP particles lose electric contact between each other resulting in capacity fade. This was confirmed from the SEM images of SIP and SIP-C electrodes after 200 cycles of charging and discharging (**Figure S4**). Figure S4a-b showed the presence of sub-microscopic cracks on the surface of SIP, while the SIP-C electrode did not show any cracks (Figure S4c-d), indicating better structural stability of SIP-C during cycling.

The cyclic voltammetry (CV) curve of the SIP-C sample (*vs.* Na/Na^+) in **Figure 5**a shows two regions, representing the redox couples for Fe^{3+}/Fe^{2+} (< 3.0 V) and Fe^{3+}/Fe^{4+} (> 3.0 V). In Figure 5b, the presence of the Fe^{3+}/Fe^{4+} redox couple was observed. These redox couples showed minimal voltage hysteresis, indicating good reversible property of SIP-C in this wide potential window from 1.5 to 4.2 V. Figure 5c shows the charge/discharge characteristics of SIP-C in the potential range from 1.5 to 4.2 V (*vs.* Na/Na^+) at 0.1 C. The charge/discharge plateaus were found to be in agreement with the redox peaks observed in the CV (Figure 5a).

For the NASICON crystal structure, it is anticipated that the Na^+ ions can occupy two interstitial sites during the charge/discharge process in the given potential range, i.e. Na(I) (six-fold coordination situated between two adjacent lantern units) and/or Na(II) (eight-fold coordination between two PO_4 tetrahedral). The charge/discharge profile for the initial cycles demonstrating the reversibility of the SIP-C sample at 1 C is shown in **Figure S5**. To distinguish the capacity contribution of Fe^{3+}/Fe^{4+} and Fe^{3+}/Fe^{2+}, the galavanostatic charge/discharge studies from 1.5 to 3.0 V and from 3.0 to 4.2 V (*vs.* Na/Na^+) were carried out (**Figure S6**). The capacities of SIP-C above and below 3.0 V were found to be ~22 and 68 mAh g^{-1}, respectively, at 1 C. In addition, the cycling performance of SIP-C at 1 C from 3.0 to

4.2 V was found to be promising (~99 % capacity retention at the end of 100 cycles. Figure S6b). Furthermore, the stability of Fe^{4+} state in SIP-C was confirmed by the self-discharge test. After the SIP-C was charged to 4.2 V and kept for 15 days in the charged state, > 3.4 V was retained, indicating the low self-discharge property and the stability of Fe^{4+} state. In contrast, the previously reported α-$NaFeO_2$ layered system showed the rapid self-discharge from 0.5 state of charge. [11] The formation of stable Fe^{4+} oxidation state in the SIP-C was further confirmed by the *ex-situ* XPS study. Figure 5d showed the Fe 2p XPS analysis of the prepared cell, containing multiplet of Fe^{3+} states. However, the de-convoluted XPS data of the cell charged at 4.2 V showed peaks for both Fe^{3+} and Fe^{4+} states (Figure 5e). Moreover, to further confirm the formation of Fe^{4+} state, the *ex-situ* X-ray absorption near edge structure (XANES) measurement [32] was carried out on the as-prepared and the charged SIP-C cells. The Fe K-edge XANES spectra (Figure 5f) showed the overall edge position of the charged electrode shifted to the higher energy as compared to the as-prepared electrode due to the increase in binding energy for the Fe electrons. The valence of Fe in the as-prepared SIP-C sample is +3. For the charged electrode, the obvious absorption edge shift to the higher energy position indicates the formation of Fe^{4+}. Furthermore, the stability of the Fe^{4+} state in a charged cell was analyzed after 2 weeks of self-discharge (**Figure S7**). The absorption edge position of the self-discharged electrode is higher than that of the as-prepared SIP-C sample, indicating that the average valence of iron is above 3, confirming the stable formation of Fe^{3+}/Fe^{4+}redox couple.

The schematic energy diagram of Fe^{3+}/Fe^{4+} redox couple against Na/Na^+ is illustrated in **Figure S8**. In general, an anode with electrochemical potential (μ) above the lowest unoccupied molecular orbital (LUMO) will reduce the electrolyte, unless a passivation layer like solid electrolyte interface (SEI) layer creates a barrier to the electron transfer from the anode to the LUMO of electrolyte. On the other hand, a cathode with a μ below the highest occupied molecular orbital (HOMO) will oxidize the electrolyte unless a passivation layer

blocks the electron transfer from the HOMO of electrolyte to the cathode. [33] Therefore, to have a thermodynamically stable system, it is very important to locate the electrochemical potentials of cathode and anode within the electrolyte window. Generally, the open circuit voltage (V_{oc}) of a cell can be described in Equation (1): [33]

$$eV_{oc} = \mu_{Anode} - \mu_{Cathode} \quad (1)$$

where e is the magnitude of electron charge. The V_{oc} is mainly constrained by the electrochemical window (VE), which is always less than or equal to the electrochemical window. However, in most cases, the electrochemical cell is kinetically stable beyond the V_{oc} (provided that the difference between the V_{oc} and VE should not be too large) because of the formation of SEI layer at the interface of electrode/electrolyte. In the present study, the V_{oc} was observed to be > 3.0 V, which is much higher than the potential of the Fe^{3+}/Fe^{2+} redox couple (2.5 V), demonstrating a stable kinetics above 3 V. The driving force for the formation of Fe^{4+} state in the present study is considered to be the continuous charging of SIP-C electrode above 3 V. The charging of SIP-C electrode above 3 V normally favors the formation of Fe^{4+}. The stability of the formed Fe^{4+} state depends on the structural redistribution of the material and the electrolyte stability. The NASICON structure is usually considered to be stable, owing to their open three-dimensional (3D) framework feature, high ionic conductivity, and a small phase related volume change during the sodium intercalation/de-intercalation processes. In general, the instability of the redox couple occurs because of two main reasons: (1) the redox potential is located away from that of Na/Na^+ and located above the electrochemical window of the electrolyte, which cannot guarantee the neutrality of the electrolyte versus the cathode; (2) The redox couple potential is too close to that of Na/Na^+, which results in a too low voltage of the cell. Such behavior is related to the high spin configuration and instability. In the present study, the Fe^{3+}/Fe^{4+} (3.0-3.6 V) redox couple is located in an ideal potential range, which we believe is the reason for the better stability of the SIP-C system. Moreover, the observed high reversibility of the

charge/discharge processes is due to the minimal volume change associated with the NASICON structure and the similarity of the crystal structure of charged and discharged states. Unlike the high capacity cathodes used for SIBs,[34, 35] we believe that this Fe^{3+}/Fe^{4+} redox couple can be beneficial for improving the energy density of the SIBs by means of improved voltage in combination with stable anodes.[36, 37]

In summary, we have investigated the reversible nature of Fe^{3+}/Fe^{4+} redox couple and the electrochemical performance of $Na_3Fe_2(PO_4)_3$ cathodes. The NASICON-based $Na_3Fe_2(PO_4)_3$ wrapped with the conducting carbon, *i.e.* SIP-C, exhibited a discharge specific capacity of ~109 mAh g^{-1} and cycling stability with > 96% capacity retention after 200 cycles. The CV, XPS, and XANES analyses revealed the formation of Fe^{4+} oxidation state in the charged cell. After examining the self-discharge behavior, the cycling performance and the coulombic efficiency of the charged cell, we confirmed the reversibility of Fe^{3+}/Fe^{4+} redox couple in the SIP-C. We believe that the present study can open up new strategy for the development of stable Fe^{3+}/Fe^{4+} redox couple based cathode materials for SIBs. Although the present study shows potential benefit of $Na_3Fe_2(PO_4)_3$ in improving the operating voltage, there are plenty of other scopes to further improve the rate and cycling stability of this material. Currently, our group is pursuing this by means of tuning the surface chemistry and morphology of the electrode. Moreover, an appropriate active component that makes of the counter electrode also needs detailed investigation in order to gain deep understanding of electrochemical performance of a full working cell.

Supporting Information

Supporting Information is available from the Wiley Online Library or from the author.

Acknowledgments

This work was supported by MOE under AcRF Tier 2 (ARC 26/13, No. MOE2013-T2-1-034; ARC 19/15, No. MOE2014-T2-2-093; MOE2015-T2-2-057) and AcRF Tier 1 (RG5/13), and NTU under Start-Up Grant (M4081296.070.500000) in Singapore. The Cooperative Research

Centre for Advanced Automotive Technology, Department of Industry and Science of the Australian Government, is also gratefully acknowledged for financial support (project code: Auto CRC 1-111).

Received: ((will be filled in by the editorial staff))
Revised: ((will be filled in by the editorial staff))
Published online: ((will be filled in by the editorial staff))

References

[1] H. Kim, I. Park, S. Lee, H. Kim, K. Y. Park, Y.U. Park, H. Kim, J. Kim, H. D. Lim, W. S. Yoon, K. Kang, *Chem. Mater.* **2013**, *25*, 3614.

[2] X. L. Wu, Y. G. Guo, J. Su, J. W. Xiong, Y. L. Zhang, L. J. Wan, *Adv. Energy Mater*. **2013**, *3*, 1155.

[3] B. Kang, G. Ceder, Nature **2009**, *458*, 190.

[4] A. E. Bocquet, A. Fujimori, T. Mizokawa, T. Saitoh, H. Namatame, *Phys. Rev. B.* **1992**, *45*, 1561.

[5] M. Hibino, T. Kimura, Y. Suga, T. Kudo, N. Mizuno, Sci. *Rep.* **2012**, *601*, 1.

[6] N. Yabuuchi, M. Kajiyama, J. Iwatate, H. Nishikawa, S. Hitomi, R. Okuyama, R. Usui, Y. Yamada, S. Komaba, *Nat. Mater*. **2012**, *11*, 512.

[7] B. L. Ellis, W. R. M. Makahnouk, Y. Makimura, K. Toghill, L. F. Nazar, *Nat. Mater*. **2007**, *6*, 749.

[8] S. Kikkawa, S. Miyazaki, M. Koizumi, *Mat. Res. Bull*. **1985**, *20*, 373.

[9] Y. Takeda, K. Nakahara, M. Nishijima, N. Imanishi, O. Yamamoto, *Mat. Res. Bull*. **1994**, *29*, 659.

[10] S. Okada, Y. Takahashi, T. Kiyabu, T. Doi, J. Yamaki, T. Nishida, 210th ECS meeting, Abstract #201. Cancun, Mexico **2006**.

[11] E. Lee, D. E. Brown, E. E. Alp, Y. Ren, J. Lu, J. J. Woo, C. S. Johnson, *Chem. Mater*. **2015**, *27*, 6755.

[12] Y. Jiang, L. Zeng, J. Wang, W. Li, F. Pana, Y. Yu, *Nanoscale* **2015**, *7*, 14723.

[13] A. Langrock, Y. Xu, Y. Liu, S. Ehrman, A. Manivannan, C. Wang, *J. Power Sources* **2013**, *223*, 62.

[14] J. Kim, D. H. Seo, H. Kim, I. Park, J. K.Yoo, S. K. Jung, Y. U. Park, *Energy Environ. Sci*. **2015**, *8*, 540.

[15] H. Kim, R. A. Shakoor, C. Park, S. Y. Lim, J. S. Kim, Y. N. Jo, W. Cho, K. Miyasaka, R. Kahraman, Y. Jung, J. W. Choi, *Adv. Funct. Mater*. **2013**, *23*, 1147.

[16] S. M. Oh, S. T. Myung, J. Hassoun, B. Scrosati, Y. K. Sun, *Electro chem Commun*. **2012**, *22*, 149.

[17] V. Mathew, S. Kim, J. Kang, J. Gim, J. Song, J. P. Baboo, D. Park, J. Han, L. Gu, Y. Wang, Y. S. Hu, Y. K. Sun, J. Kim, *NPG Asia Mater*. **2014**, *6*, e138.

[18] Y. Liu, Y. Xu, X. Han, C. Pellegrinelli, Y. Zhu, H. Zhu, J. Wan, A. Chung, O. Vaaland, C. Wang, L. Hu, *Nano Lett*. **2012**, *12*, 5664.

[19] K. Zaghib, J. Trottier, P. Hovington, F. Brochu, A. Guerfi, A. Mauger, C. M. Julien, *J Power Sources* **2011**, *196*, 9612.

[20] B.L. Ellis, W. R. M. Makahnouk, W. N. R. Weetaluktuk, D. H. Ryan, L. F. Nazar, *Chem. Mater.* **2010**, *22*, 1059.

[21] N. S. Choi, J. G. Han, S.Y. Ha, I. Parka, C. K. Back, *RSC Adv*. **2015**, *5*, 2732.

[22] C. Masquelier, C. Wurm, J. R.Carvajal, J. Gaubicher, L.Nazar, *Chem. Mater*. **2000**, *12*, 525.

[23] W. Song, X. Ji, Z. Wu, Y. Zhu, Y. Yang, J. Chen, M. Jing, F. Li, C. E. Banks, *J. Mater. Chem. A* **2014**, *2*, 5358.

[24] G. Butt, N. Sammes, G. Tompsett, A. Smirnova, O. Yamamoto, *J. Power Sources* **2004**, *134*, 72.

[25] M. Barj, G. Lucazeau, C. Delmas, *J. Solid State Chem*. **1992**, *100*, 141.

[26] A. Shalaby, D. Nihtianova, P. Markov, A. D. Staneva, R. S. Iordanova, Y. B. Dimitriev, Bulg. *Chem. Commun.* **2015**, *47*, 291.

[27] N.R. Wilson, P.A. Pandey, R. Beanland, R.J. Young, I.A. Kinloch, L. Gong, Z. Liu, K. Suenaga, J.P. Rourke, S. J. York, J. Sloan, *ACS Nano* **2009**, *3*, 2547.

[28] W.D. Callister, D.G. Rethwisch, Materials science and engineering: An Introduction, 9th Ed., Wiley, **2013**, p. 333.

[29] S. H. Avner, Introduction to physical metallurgy, 2nd Ed., McGraw-Hill, **1974**, p. 225.

[30] P. Arorat, R.E. White, M. Doyle, *J. Electrochem. Soc*. **1998**, *145*, 3647.

[31] J. Xu, R. D. Deshpande, J. Pan, Y. T. Cheng, V.S. Battaglia, *J. Electrochem. Soc.* **2015**, *162*, A2026.

[32] Y. Du, Y. Zhu, S. Xi, P. Yang, H. O. Moser, M. B. H. Breese, A. Borgna, *J. Synchrotron Rad*. **2015**, *22*, 839.

[33] J. B. Goodenough, Y. Kim, *Chem. Mater.* **2010**, *22*, 587.

[34] S. Yuan, Y. B. Liu, D. Xu, D. L. Ma, S. Wang, X. H. Yang, Z. Y. Cao, X. B. Zhang, *Adv. Sci.* **2015**, *1400018*, 1.

[35] D. L. Ma, H. G. Wang, Y. Li, D. Xu, S. Yuan, X. L. Huang, X. B. Zhang, Y. Zhang, *Nano Energy*, **2014**, *10*, 295.

[36] T. Sun, Z. Li, H. Wang, D. Bao, F. Meng, X.B. Zhang, *Angew. Chem. Int. Ed*. **2016**, *55*, 1.

[37] S. Yuan, X. L. Huang, D. L. Ma, H.G. Wang, F. Z. Meng, X.B. Zhang, *Adv. Mater.* **2014**, *26*, 2273.

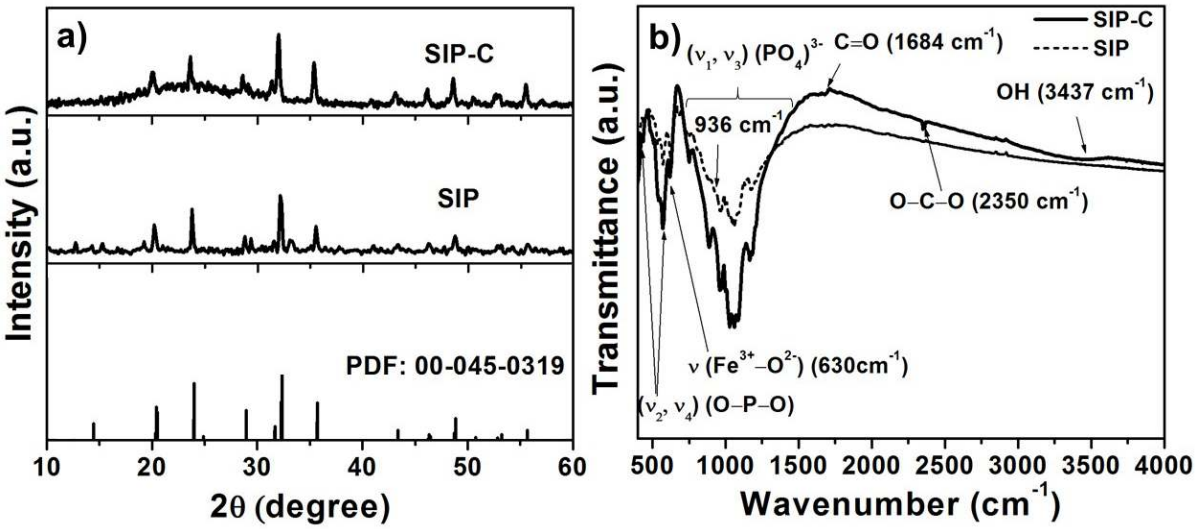

Figure 1. (a) XRD (PDF card No.: 00-045-0319) and (b) FTIR analyses of SIP and SIP-C samples.

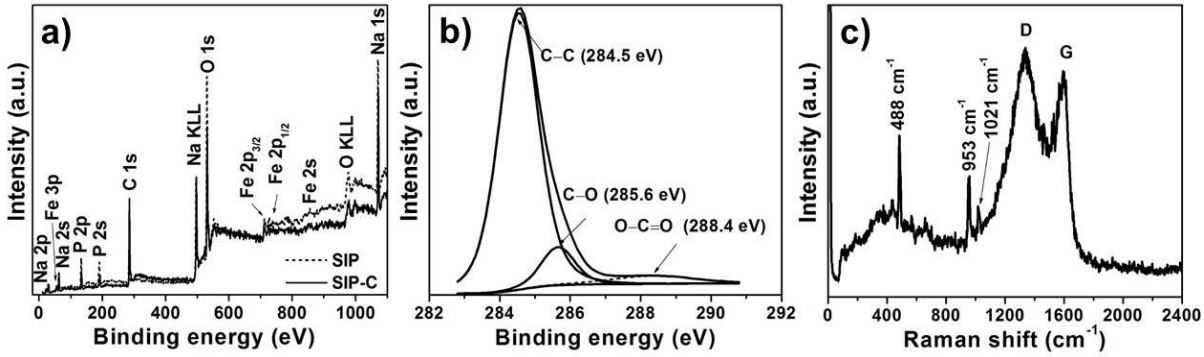

Figure 2. (a) XPS spectra of SIP and SIP-C samples, (b) de-convoluted XPS C 1s spectra of SIP-C sample and (c) Raman spectrum of SIP-C sample.

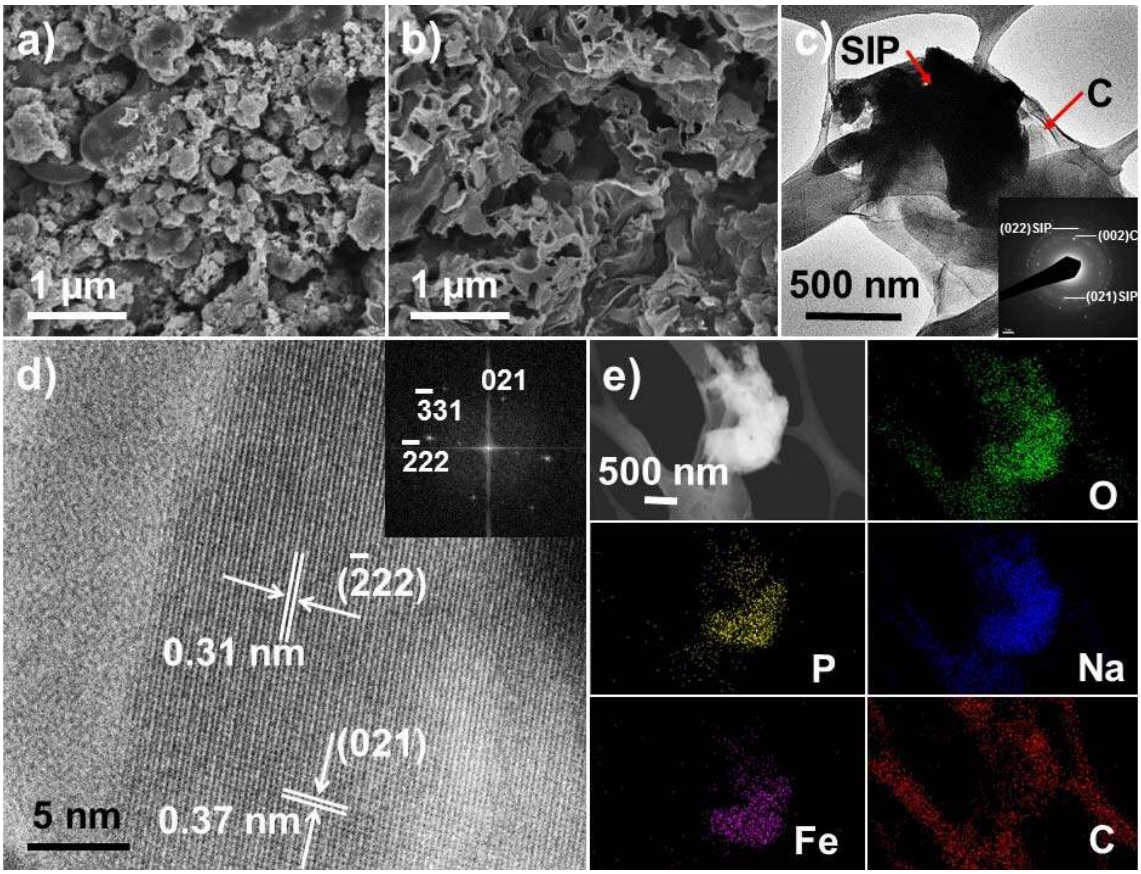

Figure 3. (a) SEM image of SIP, (b) SEM and (c) TEM and (d) HRTEM image of SIP-C. Inset in (c): the SAED pattern and inset in (d) FFT pattern of SIP-C, (e) STEM image and the corresponding EDS mapping of SIP-C.

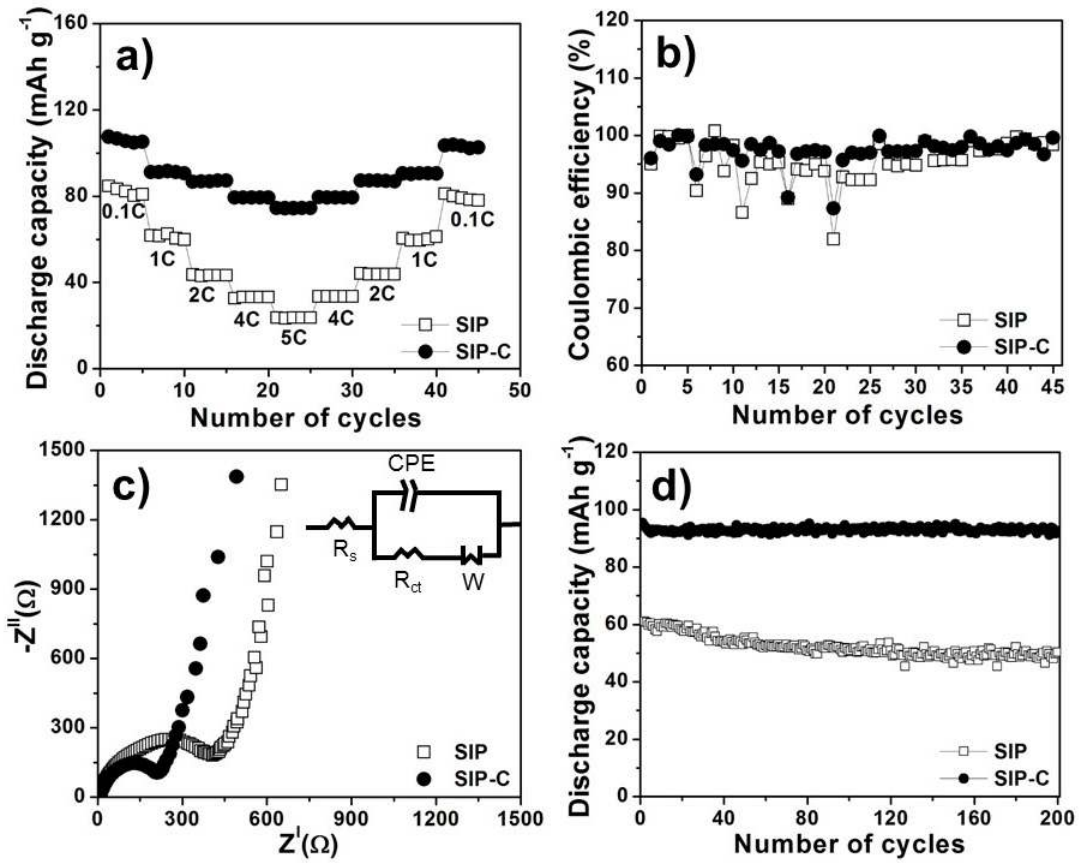

Figure 4. (a) Rate capability, (b) coulombic efficiency, (c) Nyquist plots (inset: the equivalent circuit) and (d) cycling stability of SIP and SIP-C samples at 1 C.

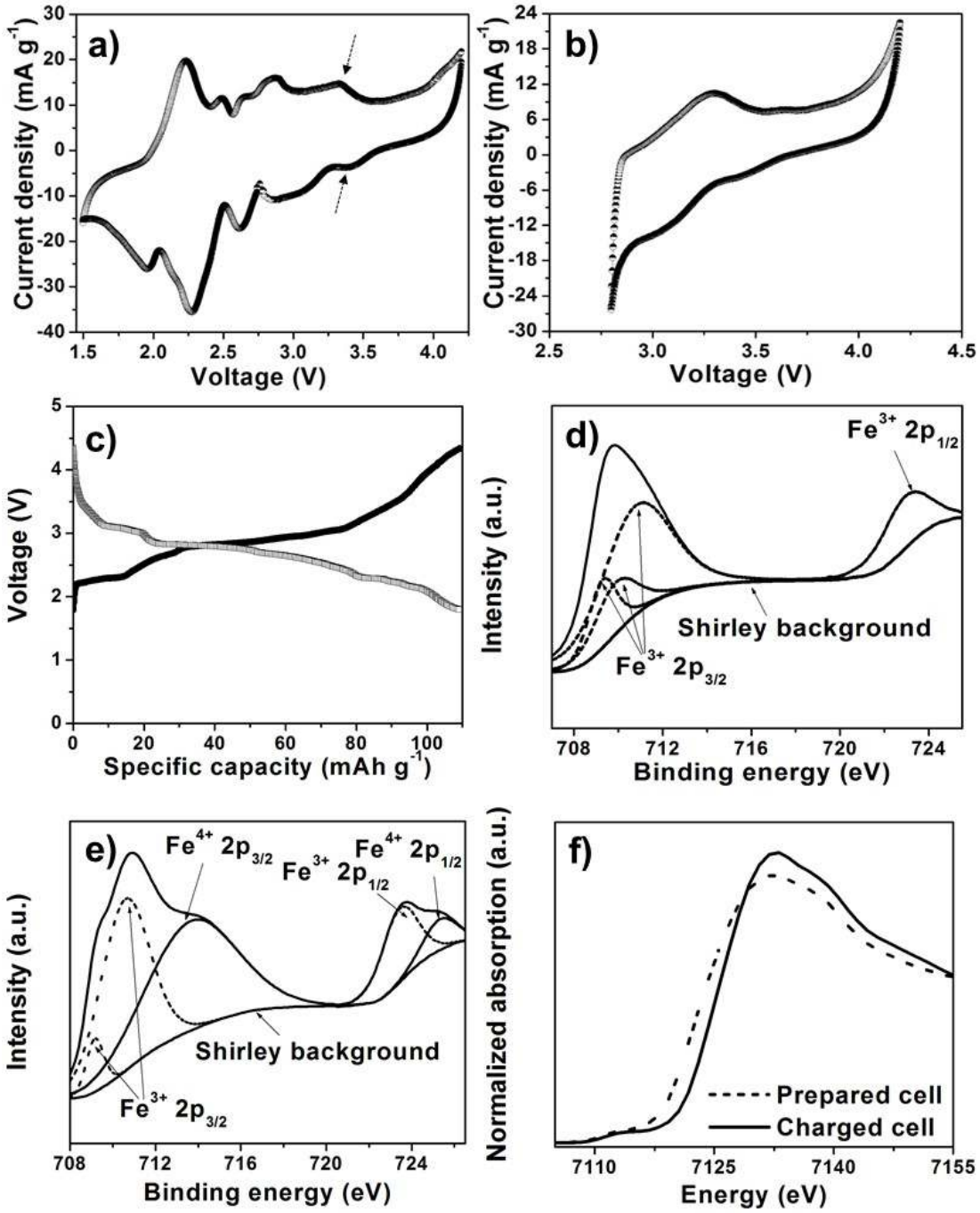

Figure 5. CV curves of SIP-C obtained at scan rate of 0.1mV s^{-1} in the potential window of (a) 1.5 to 4.2 V (the arrows indicate the Fe^{3+}/Fe^{4+} redox couple) and (b) 2.8 to 4.2 V. (c) Charge/discharge profile of SIP-C. Fitted XPS curves of (d) the prepared SIP-C electrode and (e) after charging to 4.2 V. (f) Fe K-edge XANES spectra of the prepared and charged SIP-C electrodes.

The table of content

The methodology employed here utilizes the 3D NASICON-type sodium iron phosphate wrapped with conducting carbon network to generate a stable Fe^{3+}/Fe^{4+} redox couple at ~3.4 V (*vs.* Na/Na^{+}), thereby exhibiting higher operating voltage and energy density of sodium-ion batteries. This new class of sodium iron phosphate wrapped by carbon also displayed a cycling stability with > 96% capacity retention after 200 cycles.

Keyword: Sodium iron phosphate, specific capacity, Fe^{3+}/Fe^{4+} redox couple, sodium-ion batteries, cycling

Authors: Ranjusha Rajagopalan, Bo Chen, Zhicheng Zhang, Xing-Long Wu, Yonghua Du, Ying Huang, Bing Li, Yun Zong, Jie Wang, Gwang-Hyeon Nam, Melinda Sindoro, Shi Xue Dou,* Hua Kun Liu,* Hua Zhang*

Improved Reversibility of Fe^{3+}/Fe^{4+} Redox Couple in Sodium Super Ion Conductor-Type $Na_3Fe_2(PO_4)_3$ for Sodium-Ion Batteries

TOC figure: